Cs₃Cu₂I₅ Single Crystal for Efficient Direct X-ray Detection

Wei Qinhua

College of Materials and Chemistry, China Jiliang University, Hangzhou 310018, China

Fan Xiongsheng

Materials Interfaces Center,Shenzhen Institute of Advanced Technology, Chinese Academy of Sciences

Xiang Peng

College of Materials and Chemistry, China Jiliang University

Qin Laishun

College of Materials and Chemistry, China Jiliang University

Liu Wenjun

Materials Interfaces Center, Shenzhen Institute of Advanced Technology, Chinese Academy of Sciences

Tongyu Shi

Shenzhen Institute of Advanced Technology, Chinese Academy of Sciences

Yin Hang

College of Materials and Chemistry, China Jiliang University

Peiqing Cai

China Jiliang University

Tong Yufeng

College of Materials and Chemistry, China Jiliang University

Tang Gao

College of Materials and Chemistry, China Jiliang University

Zugang Liu

China Jiliang University   https://orcid.org/0000-0001-9874-5032

Paul Chu

City University of Hong Kong   https://orcid.org/0000-0002-5581-4883

Hongsheng Shi

Xinjiang Technical Institute of Physics & Chemistry, CAS

Liu Yanliang

Materials Interfaces Center, Shenzhen Institute of Advanced Technology, Chinese Academy of Sciences

Xue-Feng Yu (✉ xf.yu@siat.ac.cn)

Shenzhen Institute of Advanced Technology, Chinese Academy of Sciences   https://orcid.org/0000-0003-2566-6194

Article

Abstract

Low-dimensional copper-based halide perovskite single crystals are considered excellent scintillators for indirect X-ray detection, but their potential in direct X-ray detection has not been investigated. Herein, high-quality pure $Cs_3Cu_2I_5$ and Li-doped $Cs_3Cu_2I_5$:Li single crystals are grown by the Bridgman method. The Li^+ dopant enhances the photoelectric properties of the $Cs_3Cu_2I_5$ single crystal by extending the carrier life time, improving the carrier mobility from 6.49 to 9.52 $cm^2V^{-1}s^{-1}$, and increasing the mobility-lifetime ($\mu\tau$) product from 1.4×10^{-4} to 2.9×10^{-4} cm^2V^{-1}. The sensitive direct X-ray detector with a vertical device configuration of Au/$Cs_3Cu_2I_5$:Li single crystal/PCBM/Au is fabricated and demonstrated to have a high sensitivity of 831.1 $\mu C\ Gy_{air}^{-1}\ cm^{-2}$ and low detection limit of 34.8 $nGy_{air}\ s^{-1}$. Furthermore, the detector shows fast response, negligible baseline current drift and excellent stability upon X-ray illumination.

Introduction

X-ray imaging is widely used in medical diagnosis and treatment[1], such as digital radiographic (DR)[2] and computerized tomography (CT)[3]. However, a high radiation dose poses health and cancer hazards and so low-dose X-ray imaging is highly desirable. There are indirect and direct approaches in X-ray imaging [4]. The indirect converter with a typical sensitivity of 0.3 $\mu C\ Gy_{air}^{-1}\ cm^{-2}$ is more prevalent but suffers from low spatial resolution and quantum efficiency due to inevitable visible light scattering. On the other hand, although the direct converter composed of semiconducting materials is able to monitor the X-ray excited charges[5] with higher sensitivity and spatial resolution in low-dose X-ray imaging, conventional semiconducting materials have some limitations and deficiencies. For instance, Si[6] and α-Se[7] lack sufficient stopping power for X-ray, consequently hindering operation in the high-energy range and HgI_2[8] detectors are plagued by the large leakage currents and low stability. CdZnTe[9] has shown great potential in room-temperature X-ray detection, there are drawbacks such as non-uniform charge transport and larger noise. In addition, the complicated preparation process and high fabrication cost pose practical challenges [10].

Recently, halide perovskites possessing attractive properties, such as large radiation attenuation coefficients, high carrier mobility life product ($\mu\tau$), tunable band gap and bulk resistivity, and high fluorescence yields[11,12], have been proposed to be efficient direct X-ray irradiation detectors[13]. However, common lead halide organic-inorganic perovskites suffer from the poor environmental stability and toxicity of lead-based salts[14,15], Lead-free Copper-based halide perovskites show large radiation attenuation, high photoluminescence quantum yield (PLQY), lack of self-absorption, and good air-stability[16][17][18], rendering it suitable for X-ray imaging and γ-ray detection, especially the zero-dimensional (0D) $Cs_3Cu_2I_5$ crystal. For example, clear reconstructed 3D snail CT images have been obtained by the $Cs_3Cu_2I_5$ nanocrystal-based fiber-optic panel[19]. The $Cs_3Cu_2I_5$:Tl single crystal simultaneously exhibits high scintillation yield and remarkable energy resolution under [137]Cs γ-ray radiation in conjunction with low detection limit and afterglow in indirect X-ray detection[20,21]. The Li^+-

doped $Cs_3Cu_2I_5$ single crystal also has an excellent figure-of-merit, which can be used in the field of dual gamma-ray and neutron detection[22]. Moreover, the $Cs_3Cu_2I_5$:In single crystal-based imaging system has excellent spatial resolution[23]. Because of the $Cs_3Cu_2I_5$ is constructed with $[Cu_2I_5]^{3-}$ coordinated polyhedron, spatially separated by Cs^+ that only serves as a skeleton to form the localized electronic structure[24]. The beneficial disrupted ion migration channels avoid the dark current noise and baseline drift problems at high bias voltages[25], thereby maintaining the resolution and stability of the $Cs_3Cu_2I_5$-based detector. In direct X-ray detection by the $Cs_3Cu_2I_5$ single crystal, the semiconductor converts X-ray into electrical signals with high sensitivity and spatial resolution. However, because of the larger band-gap of the $Cs_3Cu_2I_5$ single crystal and poor electrical properties, the capability of $Cs_3Cu_2I_5$ in direct X-ray detection has not been studied systematically.

In this work, the strategy of Li^+-doped was adopted to enhance the photoelectric properties of $Cs_3Cu_2I_5$ single crystal by extending the carrier life time and improving the carrier mobility. The pure $Cs_3Cu_2I_5$ and Li-doped $Cs_3Cu_2I_5$:Li single crystals with a diameter of 12 mm are prepared by the Bridgman method and their properties pertaining to direct X-ray detection are investigated. The pure $Cs_3Cu_2I_5$ single crystal has moderate electronic properties such as carrier mobility of 6.49 $cm^2V^{-1}s^{-1}$ and mobility-lifetime ($\mu\tau$) product of 1.4×10^{-4} cm^2V^{-1}. Doping with lithium improves optical-electrical properties including bigger carrier mobility of 9.52 $cm^2V^{-1}s^{-1}$ and mobility-lifetime ($\mu\tau$) product of 2.9×10^{-4} cm^2V^{-1}. Subsequently, the direct X-ray detector assembled with the $Cs_3Cu_2I_5$:Li single crystal shows a high sensitivity of 831.1 μC Gy_{air}^{-1} cm^{-2} and low detection limit of 34.8 nGy_{air} s^{-1}. The detector also exhibits excellent stability with negligible current drifts during continuous X-ray exposure.

Results

Crystal Growth and First-Principle Calculation. Figure 1a presents the schematic diagram of the custom vertical Bridgman growth furnace with three zones. The temperature gradient can be adjusted from 10°C to 25°C for a length of 40 mm and the descending speed can be adjusted up to 0.001 mm/h. The pure $Cs_3Cu_2I_5$ and 2.5 at% Li^+-doped $Cs_3Cu_2I_5$:Li single crystals are grown by the self-seeding Bridgman technique with a capillary tube. The as-grown $Cs_3Cu_2I_5$:Li single crystal ingots with a diameter of 12 mm and transparent machined sample without cracks and visible inclusions are exhibited in Fig. 1a. The actual Li^+ doped concentration was confirmed by ICP-OES measurement. The actual Li^+ concentration is about 0.92 at% for 2.5 at% Li^+-doped $Cs_3Cu_2I_5$ crystal, indicating that the Li^+ was introduced successfully. The powder XRD pattern of the polycrystalline $Cs_3Cu_2I_5$:Li can be indexed to the pure $Cs_3Cu_2I_5$ PDF card #45−0077 revealing the absence of impurity phases like CsI or CuI, as shown in Fig. 1b. $Cs_3Cu_2I_5$ crystallizes into the orthorhombic space group of Pnma at room temperature. Consider for the radius of Li^+ (0.59 Å) is closer to that of Cu^+ (0.60 Å), the Li^+ exhibits a tendency to substitute for the Cu^+ site.

To gain mechanistic insights into the optical properties of the Li$^+$ doped effect on Cs$_3$Cu$_2$I$_5$ single crystals, the electronic band structures are derived by density-functional theory (DFT) calculation with the PBE hybrid functional. Both the valence band edges in Figs. 1c and d are completely flat between the F and Z direction, which differ from the large bandwidth and dispersion band edges of conventional 3D structures. The direct band-gap of Cs$_3$Cu$_2$I$_5$ is smaller than that of Li$^+$-doped Cs$_3$Cu$_2$I$_5$, indicating a broken symmetry after introducing Li$^+$ to enlarge the band-gap. According to the DOS and PDOS map, the valence band maximum (VBM) is mainly contributed by the I-p orbitals and some Cu-d orbitals. Whereas, the conduction band minimum (CBM) density states are mainly composed of Cu-4s and I-5p orbitals. The flat VBM energy profiles of pure and Li$^+$-doped Cs$_3$Cu$_2$I$_5$ indicate localized charge distributions corresponding to the charge density maps of VBM and CBM (Figs. 1e and f). In particular, most of the charges of Li$^+$-doped Cs$_3$Cu$_2$I$_5$ transfer from the [LiI$_6$] octahedrons to [CuI$_6$] octahedrons while some charges transfer from the metal to halide upon photoexcitation from VBM to CBM as shown in Fig. 1f marked with red circle. Compared to the pure Cs$_3$Cu$_2$I$_5$, more prominent charge transfer in Li$^+$-doped Cs$_3$Cu$_2$I$_5$ enhances the conductivity and doping with Li extends the carrier lifetime and improves the carrier mobility.

Optical properties of pure and Li $^+$ -doped Cs $_3$ Cu $_2$ I $_5$ single crystal. The survey XPS spectrum of Cs$_3$Cu$_2$I$_5$:Li crystal in Fig. 2a reveals the C 1s, Cs 3d, Cu 2p, and I 3d components and the high-resolution spectra are conducted to validate the chemical states of matrix ions. The binding energies of Cu 2p$_{1/2}$ and Cu 2p$_{3/2}$ are consistent with Cu-I bond and demonstrate the presence of Cu$^+$ in the host. The satellite peak for the Cu^{2+} oxidation state cannot be observed. The binding energies of the 3d orbital correspond to the Cs and I + 1 and − 1 states, respectively. Compared to the XPS result of Cs$_3$Cu$_2$I$_5$ crystal, presenting in Figure S1, the Li$^+$ doped has no influence on chemical states of the crystal composition, except that the peaks position has a slight shift of 0.4 eV. The PLE and PL spectra of pure Cs$_3$Cu$_2$I$_5$ and Cs$_3$Cu$_2$I$_5$:Li single crystals was measured and shown in Fig. 2b while the time resolved PL decay time curves were shown in Fig. 2c. After Li$^+$ doping, the excitation (at 310 nm) and emission (at 445 nm) bands do not show obvious changes, but the decay time becomes slightly longer from 1002 ns to 1015 ns, indicating that the Li$^+$-doped Cs$_3$Cu$_2$I$_5$ crystal has a longer electron-hole recombination time. Hence, the mobility-lifetime (μτ) product increases with Li$^+$ doping boding well for direct X-ray detection. Figures 2d and e present the ultraviolet-visible absorption spectra of the pure and Li$^+$-doped Cs$_3$Cu$_2$I$_5$ sample, respectively. The inset is the Tauc plot curve converted by the Kubelka-Munk equation for the band gap calculation[26]. Both the pure and Li$^+$-doped Cs$_3$Cu$_2$I$_5$ exhibit a sharp absorption edge indicative of a direct band gap. The corresponding band gap energy (E_g) of Cs$_3$Cu$_2$I$_5$:Li is estimated to be 3.62 eV, which is bigger than that of the pure Cs$_3$Cu$_2$I$_5$ crystal (3.57 eV) and slightly exceeds that of the conventional semiconductor X-ray detector [27]. This trend is in good agreement with the DFT calculation shown in Figs. 1c and d.

Electronic properties of the Cs $_3$ Cu $_2$ I $_5$ single crystal. The carrier mobility is an important factor for X-ray detection, and the Hall-effect measurement was used to investigate the electronic properties of pure and

Cs$_3$Cu$_2$I$_5$:Li single crystal. Two samples exhibit n-type conductivity. The Cs$_3$Cu$_2$I$_5$:Li single crystal has higher carrier mobility of 9.52 cm^2 V^{-1} s^{-1} than the pure Cs$_3$Cu$_2$I$_5$ single crystal (6.49 cm^2 V^{-1} s^{-1}), and it is larger than that of Cs$_3$Bi$_2$Br$_9$ (1.54 cm^2 V^{-1} s^{-1})[28] and two times that of Cs$_2$AgBiBr$_6$ (3.17 cm^2 V^{-1} s^{-1})[29] and MAPbBr$_3$ (4.16 cm^2 V^{-1} s^{-1})[30]. It means that the Li dopant enhances the conductivity of the Cs$_3$Cu$_2$I$_5$ single crystal, and the positive effect on the conductivity is confirmed by experiments and DFT calculation.

The pure Cs$_3$Cu$_2$I$_5$ and Cs$_3$Cu$_2$I$_5$:Li single crystal ingots are machined into squares and integrated into X-ray detectors with the stacked structure of Au/Cs$_3$Cu$_2$I$_5$ or Cs$_3$Cu$_2$I$_5$:Li/PCBM/Au and level alignment as shown in Fig. 3a. Figure 3b compares the absorption coefficients of typical and potential materials for X-ray detection, which were calculated according to the photon cross-section database[31]. Since Cs$_3$Cu$_2$I$_5$ consisting of heave elements of Cs, Cu, and I have a large high density (4.52 g cm^{-3}), it has a bigger X-ray absorption coefficient than Cs$_2$AgBiBr$_6$, α-Se, and commercial silicon, and comparable with CdTe. The photoconductivity measurements are carried out to determine the optoelectronic properties of the Cs$_3$Cu$_2$I$_5$ and Cs$_3$Cu$_2$I$_5$:Li single crystal, as shown in Fig. 3c. The photocurrent response is monitored by applying a voltage ranging from 0 to 60 V and the Hecht formula is employed to fit the photocurrent-voltage curve:

$$I = I_0\mu\tau V/L^2(1-\exp(-L^2/\mu\tau V))$$

where I_0 is the saturated current, L is the thickness of the Cs$_3$Cu$_2$I$_5$ and Cs$_3$Cu$_2$I$_5$:Li single crystal, and V is the applied voltage. The μτ products of the pure Cs$_3$Cu$_2$I$_5$ and Cs$_3$Cu$_2$I$_5$:Li single crystal are determined to be 1.4×10^{-4} cm^2 V^{-1} and 2.9×10^{-4} cm^2 V^{-1}, respectively, and the bigger μτ product indicates enhanced transport of photogenerated charges. Moreover, the Cs$_3$Cu$_2$I$_5$:Li single crystal has a smaller resistivity of 2.7×10^{10} Ω cm compared to 4.3×10^{11} Ω cm of the Cs$_3$Cu$_2$I$_5$ single crystal, as shown in Fig. 3(d). Figure 3(e) shows the current density-voltage (J-V) characteristics of the X-ray detectors made of the Cs$_3$Cu$_2$I$_5$ and Cs$_3$Cu$_2$I$_5$:Li single crystals. The Cs$_3$Cu$_2$I$_5$ X-ray detector exhibits obviously lower dark currents than Cs$_3$Cu$_2$I$_5$:Li due to the high resistivity, and the dark current mainly comes from the injected current form the electrodes at the applied electric field. Meanwhile, the Cs$_3$Cu$_2$I$_5$:Li X-ray detector shows a significantly enhanced light current of 2.0×10^{-8} A cm^{-2} at an electric field of 45 V/mm, which is more than twice that of the Cs$_3$Cu$_2$I$_5$ X-ray detector of 9.3×10^{-9} A cm^{-2}. The light current originates from the X-ray excited photocurrent, and the Li-doped Cs$_3$Cu$_2$I$_5$:Li single crystal possesses higher conductivity due to enhanced charge transport thus facilitating high-sensitivity X-ray detection.

Direct X-ray detection. To obtain dynamic information from the Cs$_3$Cu$_2$I$_5$ and Cs$_3$Cu$_2$I$_5$:Li X-ray detectors, the time-resolved light current response for various X-ray dose rates from 1579 μGy$_{air}$ s^{-1} to 82 μGy$_{air}$ s^{-1} are presented in Fig. 4a, the inset is the picture of detector. Both detectors show decent response signals upon on/off X-ray switching and good linear relationship with the X-ray dose rates. The Cs$_3$Cu$_2$I$_5$:Li X-ray

detector exhibits obviously higher dark currents and light currents with larger X-ray on-off than the pure $Cs_3Cu_2I_5$ detector at an electric field of 45 V/mm, indicating the $Cs_3Cu_2I_5$:Li X-ray detector has more sensitive X-ray detection properties. Figure S2 presents the current response of the $Cs_3Cu_2I_5$ and $Cs_3Cu_2I_5$:Li detectors during X-ray on/off at different electric fields and X-ray dose rates.

To investigate the sensitivity of the $Cs_3Cu_2I_5$ and $Cs_3Cu_2I_5$:Li X-ray detectors, the X-ray generated photocurrent density are plotted as a function of X-ray dose rates as shown in Figs. 4b and 4c. The sensitivity of the X-ray detector can be calculated from the slope of the photocurrents versus X-ray dose rates plots acquired at different electric fields. The pure $Cs_3Cu_2I_5$ detector has X-ray sensitivities of 441.5 $\mu C\ Gy_{air}^{-1}\ cm^{-2}$, 363.3 $\mu C\ Gy_{air}^{-1}\ cm^{-2}$, 288.5 $\mu C\ Gy_{air}^{-1}\ cm^{-2}$, 233.1 $\mu C\ Gy_{air}^{-1}\ cm^{-2}$ and 168.9 $\mu C\ Gy_{air}^{-1}\ cm^{-2}$ at 45, 37, 30, 28 and 15 V/mm, respectively. In comparison, the $Cs_3Cu_2I_5$:Li X-ray detector shows enhanced sensitivities of 831.1 $\mu C\ Gy_{air}^{-1}\ cm^{-2}$, 661.8 $\mu C\ Gy_{air}^{-1}\ cm^{-2}$, 422.0 $\mu C\ Gy_{air}^{-1}\ cm^{-2}$, 311.5 $\mu C\ Gy_{air}^{-1}\ cm^{-2}$ and 95.6 $\mu C\ Gy_{air}^{-1}\ cm^{-2}$ at electric fields of 45, 37, 30, 28 and 15 V/mm, respectively.

The signal-to-noise ratio (SNR) is another important parameter for X-ray detection and can be calculated by the following equation:

$$SNR = I_{signal} / I_{noise} = (I_{photo} - I_{dark}) / I_{noise}$$

where I_{photo} is the average current during X-ray irradiation, I_{dark} is the average dark current derived from parallel experiments at each bias, and I_{noise} is the noise current calculated from the standard deviation of the photocurrents. The SNRs of the X-ray detectors at an electric field of 45 V/mm are plotted as a function of dose rates in Fig. 4d, and a linear dependence with X-ray dose rates is observed. According to the International Union of Pure and Applied Chemistry standard, the detector signal should maintain an SNR of over 3. The $Cs_3Cu_2I_5$:Li X-ray detector has a smaller limit-of-detection (LoD) of 34.8 $nGy_{air}\ s^{-1}$ than the pure $Cs_3Cu_2I_5$ X-ray detector of 335.1 $nGy_{air}\ s^{-1}$, which is consistent with the higher sensitivity of the $Cs_3Cu_2I_5$:Li X-ray detector. Then, we highlight the performance of perovskite based X-ray direct conversion detectors and summarize the important parameters including the $\mu\tau$ product, sensitivity, detection limit and resistivity in Table S1. The $Cs_3Cu_2I_5$:Li crystal presents good comprehensive performance.

To evaluate the detection stability under continuous operating conditions, X-ray on/off experiments are carried out at the 45 V/mm external electric field and 1579 $\mu Gy_{air}\ s^{-1}$ X-ray dose for 3600 s as shown in Figs. 4e and S3. Both the $Cs_3Cu_2I_5$ and $Cs_3Cu_2I_5$:Li X-ray detectors exhibit reproducible and stable response with small X-ray on/off changes, indicating excellent materials and working stability under continuous X-ray exposure. The temporal baseline tracking of the X-ray detectors shown in Figure S4, and the current drift (I_{drift}) can be calculated by the following equation:

$$I_{drift} = (I_t - I_0) / (E \times S \times t),$$

where I_t is the current at time t, I_0 is the current immediately after stabilization, E is the electric field, and S is the area of the device. Both the $Cs_3Cu_2I_5$ and $Cs_3Cu_2I_5$:Li X-ray detectors are able to maintain stable dark and light currents in 3600 s, and both of the $Cs_3Cu_2I_5$ and $Cs_3Cu_2I_5$:Li X-ray detectors show smaller light current drifts of 1.17×10^{-4} A cm^{-1} s^{-1} V^{-1} and 1.35×10^{-4} A cm^{-1} s^{-1} V^{-1}, indicating excellent working stability.

The X-ray imaging capability of the $Cs_3Cu_2I_5$:Li X-ray detector is assessed by x-y scanning experiments with a key containing a plastic handle and metal bit as the imaging target. As shown in Fig. 4f, the X-ray image clearly reveals a clear outline of the key consistent with the optical image in the scanning mode.

Conclusion

The pure $Cs_3Cu_2I_5$ and Li^+-doped $Cs_3Cu_2I_5$:Li single crystals are studied for high sensitivity direct X-ray detection. The high quality pure $Cs_3Cu_2I_5$ single crystal with a size of 12 mm is grown by the Bridgman method, and doped with Li^+ to form $Cs_3Cu_2I_5$:Li single crystal. The pure $Cs_3Cu_2I_5$ single crystal shows moderate electronic properties with carrier mobility of 6.49 cm^{2}V^{-1}s^{-1} and mobility-lifetime (μτ) product of 1.4×10^{-4} cm^{2}V^{-1}. In comparison, the $Cs_3Cu_2I_5$:Li single crystal has significantly enhanced optical-electrical properties such as carrier mobility of 9.52 cm^{2}V^{-1}s^{-1} and mobility-lifetime (μτ) product of 2.9×10^{-4} cm^{2}V^{-1}. The positive effect of Li^+- doped on the properties of $Cs_3Cu_2I_5$ crystal is approved by experiments and DFT calculation. The physical mechanism need to be studied further. The efficient direct X-ray detector composed of the $Cs_3Cu_2I_5$:Li single crystal (Au/$Cs_3Cu_2I_5$:Li/PCBM/Au) shows a high sensitivity of 831.1 μC Gy$_{air}^{-1}$ cm^{-2}, low detection limit of 34.8 nGyair s^{-1}, and excellent stability under continuous X-ray illumination. The results demonstrate the high potential of the $Cs_3Cu_2I_5$:Li single crystal in direct X-ray detection.

Methods

Materials. Anhydrous 99.999% pure CuI (ALDRICH) and 99.99% pure CsI and LiI (APL Engineered Materials, Inc.) were used as starting materials. The pure and 2.5at% Li^+-doped $Cs_3Cu_2I_5$ crystals were grown by the Bridgman method. Owing to the similar Shannon radii, Li^+ is assumed to substitute for Cu^+ (d^{10}). The mixture was charged into a quartz crucible with a straight capillary on the bottom. The crucible was evacuated to a pressure 5×10^{-5} Pa and sealed with an oxyhydrogen flame. The sealed ampoule was transferred to a three-zone Bridgman furnace and the temperature in the three-zone was 460°C, 480°C and 200°C, respectively. To completely melt the starting materials, the quartz crucible was held in the high-temperature zone for 40 h. The temperature gradient near the solid-liquid interface was 20 °C/cm and the quartz crucible was descended at a speed of 0.5-1 mm/h. Finally, the furnace cooled to room temperature in 60 h to obtain the $Cs_3Cu_2I_5$ single crystal.

Material characterization. The crystal structure and phases were determined on the SmartLab SE X-ray diffractometer with Cu Kα radiation (λ = 0.1541 nm). Inductively coupled plasma optical emission spectrometry (ICP-OES) (Agilent Technologies 5100) and X-ray photoelectron spectroscopy (XPS) (Thermo Scientific K-Alpha) were carried out to determine the chemical composition. The electronic properties were evaluated by Hall-effects using the PPMS-9 comprehensive physical property measurement system as well as photoconduction measurements. The photoluminescence excitation (PLE) spectra, photoluminescence (PL) spectra, and decay time data were obtained on an FLS1000 spectrometer with a pulsed nano-LED under UV light irradiation. The absorption spectra were acquired on the ultraviolet-visible spectrophotometer (UV2600, SDPTOP).

Computation details. The density functional theory computations were performed using the Vienna Ab-initio Simulation Package(VASP)[32][33][34][35]. The hybrid exchange-correlation functional Perdew, Burke, and Ernzerhof (PBE)[36] together with the projected augmented wave (PAW) potentials[37,38] was employed in the current calculations to better reproduce the band structures[39]. The total density of states (DOS) and projected DOS (PDOS) vacancy defects of Cs, Cu, Li and I were calculated by the DFT-PBE level. The wavefunctions expanded in plane waves were cut off to a 550 eV kinetic energy and the Brillouin zone was sampled using a Γ-centred 2×2×2 k-mesh, which was examined to have good convergence against denser k-points.

Detector performance. The X-ray detection properties of the detector were evaluated using an X-ray generation system for medical imaging (Varex, G242, 18932-M8, USA) at an accelerating voltage of 50 kV and currents are ranging from 10 to 200 uA. The dose rate of the X-rays was calibrated with an X2 CT dosimeter (Unfors Raysafe, Sweden). During the measurement, the environment was kept dark and the external electrical bias and current were recorded by the PDA FS380 semiconductor analyzer. The X-ray imaging capability of the detector was demonstrated by moving the object between the detector (1 mm^2) and X-ray beam (1.62 mGy$_{air}$ s^{-1}) using a self-assembled x-y scanning system consisting of a motorized linear displacement stage (Newport, M-IMS400CC. A motorized linear displacement stage combined with a motion controller (Newport, M-IMS400CC) was used to control scanning along the x and y axes.

Declarations

References

1. Ou, X. *et al.* Recent Development in X-Ray Imaging Technology: Future and Challenges. *Research* 2021, 9892152, doi:10.34133/2021/9892152 (2021).

2. Lee, S. M. *et al.* Deep Learning Applications in Chest Radiography and Computed Tomography: Current State of the Art. Journal of Thoracic Imaging **34** (2019).

3. Mei, X. *et al.* Artificial intelligence–enabled rapid diagnosis of patients with COVID-19. Nature Medicine **26**, 1224–1228, doi:10.1038/s41591-020-0931-3 (2020).

4. Wu, H., Ge, Y., Niu, G. & Tang, J. Metal Halide Perovskites for X-Ray Detection and Imaging. Matter **4**, 144–163, doi:https://doi.org/10.1016/j.matt.2020.11.015 (2021).

5. Wu, R. *et al.* Research progress on semiconductor materials and devices for radiation detection. Journal of Synthetic Crystals **50**, 1813–1829 (2021).

6. Guerra, M., Manso, M., Longelin, S., Pessanha, S. & Carvalho, M. L. Performance of three different Si X-ray detectors for portable XRF spectrometers in cultural heritage applications. Journal of Instrumentation **7**, C10004-C10004, doi:10.1088/1748-0221/7/10/c10004 (2012).

7. Kasap, S. O. X-ray sensitivity of photoconductors: application to stabilized a-Se. Journal of Physics D: Applied Physics **33**, 2853–2865, doi:10.1088/0022-3727/33/21/326 (2000).

8. Schieber, M. *et al.* Thick films of X-ray polycrystalline mercuric iodide detectors. Journal of Crystal Growth **225**, 118–123, doi:https://doi.org/10.1016/S0022-0248(01)00832-6 (2001).

9. Szeles, C. CdZnTe and CdTe materials for X-ray and gamma ray radiation detector applications. physica status solidi (b) **241**, 783–790, doi:https://doi.org/10.1002/pssb.200304296 (2004).

10. Zhou, Y., Chen, J., Bakr, O. M. & Mohammed, O. F. Metal Halide Perovskites for X-ray Imaging Scintillators and Detectors. ACS Energy Letters **6**, 739–768, doi:10.1021/acsenergylett.0c02430 (2021).

11. Wang, S. *et al.* Growth of metal halide perovskite materials. Science China Materials **63**, 1438–1463, doi:10.1007/s40843-020-1300-2 (2020).

12. Su, Y., Ma, W. & Yang, Y. Perovskite Semiconductors for Direct X-Ray Detection and Imaging. J. Semicond. **41**, 051204 (2020).

13. Wei, H. & Huang, J. Halide lead perovskites for ionizing radiation detection. Nature Communications **10**, 1066, doi:10.1038/s41467-019-08981-w (2019).

14. Liang, W. *et al.* Strategy of All-Inorganic $Cs_3Cu_2I_5$/Si-Core/Shell Nanowire Heterojunction for Stable and Ultraviolet-Enhanced Broadband Photodetectors with Imaging Capability. ACS Appl. Mater. Interfaces **12**, 37363–37374, doi:10.1021/acsami.0c10323 (2020).

15. Fang, S. *et al.* Rapid synthesis and mechanochemical reactions of cesium copper halides for convenient chromaticity tuning and efficient white light emission. Journal of Materials Chemistry C **8**, 4895–4901, doi:10.1039/D0TC00015A (2020).

16. Jun, T. *et al.* Lead-Free Highly Efficient Blue-Emitting $Cs_3Cu_2I_5$ with 0D Electronic Structure. Advanced Materials **30**, 1804547, doi:https://doi.org/10.1002/adma.201804547 (2018).

17. Cheng, S. *et al.* Zero-Dimensional $Cs_3Cu_2I_5$ Perovskite Single Crystal as Sensitive X-Ray and γ-Ray Scintillator. physica status solidi (RRL) – Rapid Research Letters **14**, 2000374, doi:https://doi.org/10.1002/pssr.202000374 (2020).

18. Liu, D. *et al.* A novel Li^+-doped $CsCu_2I_3$ single crystal for dual gamma–neutron detection. CrystEngComm, 25, 58, doi:10.1039/D2CE01263D (2023).

19. Zhou, J. *et al.* Solution-Processed Lead-Free Perovskite Nanocrystal Scintillators for High-Resolution X-Ray CT Imaging. Advanced Optical Materials **9**, 2002144, doi:https://doi.org/10.1002/adom.202002144 (2021).

20. Yuan, D. Air-Stable Bulk Halide Single-Crystal Scintillator $Cs_3Cu_2I_5$ by Melt Growth: Intrinsic and Tl Doped with High Light Yield. ACS Appl. Mater. Interfaces **12**, 38333 (2020).

21. Cheng, S. *et al.* Ultrabright and Highly Efficient All-Inorganic Zero-Dimensional Perovskite Scintillators. Advanced Optical Materials **9**, 2100460, doi:https://doi.org/10.1002/adom.202100460 (2021).

22. Xiang, P. *et al.* An all-inorganic Li-doped $Cs_3Cu_2I_5$ single crystal for dual gamma ray and neutron detection applications. Journal of Materials Chemistry C **10**, 15400–15407, doi:10.1039/D2TC02674K (2022).

23. Wang, Q. *et al.* Highly Resolved X-Ray Imaging Enabled by In(I) Doped Perovskite-Like $Cs_3Cu_2I_5$ Single Crystal Scintillator. Advanced Optical Materials **10**, 2200304, doi:https://doi.org/10.1002/adom.202200304 (2022).

24. Lian, L. *et al.* Efficient and Reabsorption-Free Radioluminescence in $Cs_3Cu_2I_5$ Nanocrystals with Self-Trapped Excitons. Adv. Sci. **7**, 2000195 (2020).

25. Liu, Y. *et al.* Inch-Size 0D-Structured Lead-Free Perovskite Single Crystals for Highly Sensitive Stable X-Ray Imaging. Matter **3**, 180–196, doi:10.1016/j.matt.2020.04.017 (2020).

26. Tauc, J. & Menth, A. States in the gap. Journal of Non-Crystalline Solids **8–10**, 569–585 (1972).

27. McGregor, D. & Hermon, H. Room-temperature compound semiconductor radiation detectors. *Nuclear Instruments and Methods in Physics Research Section A: Accelerators*, Spectrometers, Detectors and Associated Equipment **395**, 101–124, doi:10.1016/S0168-9002(97)00620-7 (1997).

28. Li, X. *et al.* Ultralow Detection Limit and Robust Hard X-ray Imaging Detector Based on Inch-Sized Lead-Free Perovskite $Cs_3Bi_2Br_9$ Single Crystals. ACS Appl. Mater. Interfaces **14**, 9340–9351, doi:10.1021/acsami.1c24086 (2022).

29. Pan, W. *et al.* $Cs_2AgBiBr_6$ single-crystal X-ray detectors with a low detection limit. Nature Photonics **11**, 726–732, doi:10.1038/s41566-017-0012-4 (2017).

30. Li, L. *et al.* Enhanced X-ray Sensitivity of MAPbBr$_3$ Detector by Tailoring the Interface-States Density. ACS Appl. Mater. Interfaces **11**, 7522–7528, doi:10.1021/acsami.8b18598 (2019).

31. Berger, M. J. *et al. XCOM: photon cross sections database. NIST* http://physics.nist.gov/xcom, <http://physics.nist.gov/xcom> (2013).

32. Kresse, G. & Hafner, J. Ab initio molecular dynamics for liquid metals. Physical Review B **47**, 558–561, doi:10.1103/PhysRevB.47.558 (1993).

33. Kresse, G. & Hafner, J. Ab initio molecular-dynamics simulation of the liquid-metal–amorphous-semiconductor transition in germanium. Physical Review B **49**, 14251–14269, doi:10.1103/PhysRevB.49.14251 (1994).

34. Kresse, G. & Furthmüller, J. Efficiency of ab-initio total energy calculations for metals and semiconductors using a plane-wave basis set. Computational Materials Science **6**, 15–50, doi:https://doi.org/10.1016/0927-0256(96)00008-0 (1996).

35. Kresse, G. & Furthmüller, J. Efficient iterative schemes for ab initio total-energy calculations using a plane-wave basis set. Physical Review B **54**, 11169–11186, doi:10.1103/PhysRevB.54.11169 (1996).

36. Perdew, J. P., Burke, K. & Ernzerhof, M. Generalized Gradient Approximation Made Simple. Physical Review Letters **77**, 3865–3868, doi:10.1103/PhysRevLett.77.3865 (1996).

37. Blöchl, P. E. Projector augmented-wave method. Physical Review B **50**, 17953–17979, doi:10.1103/PhysRevB.50.17953 (1994).

38. Kresse, G. & Joubert, D. From ultrasoft pseudopotentials to the projector augmented-wave method. Physical Review B **59**, 1758–1775, doi:10.1103/PhysRevB.59.1758 (1999).

39. Paier, J., Hirschl, R., Marsman, M. & Kresse, G. The Perdew–Burke–Ernzerhof exchange-correlation functional applied to the G2-1 test set using a plane-wave basis set. The Journal of Chemical Physics **122**, 234102, doi:10.1063/1.1926272 (2005).
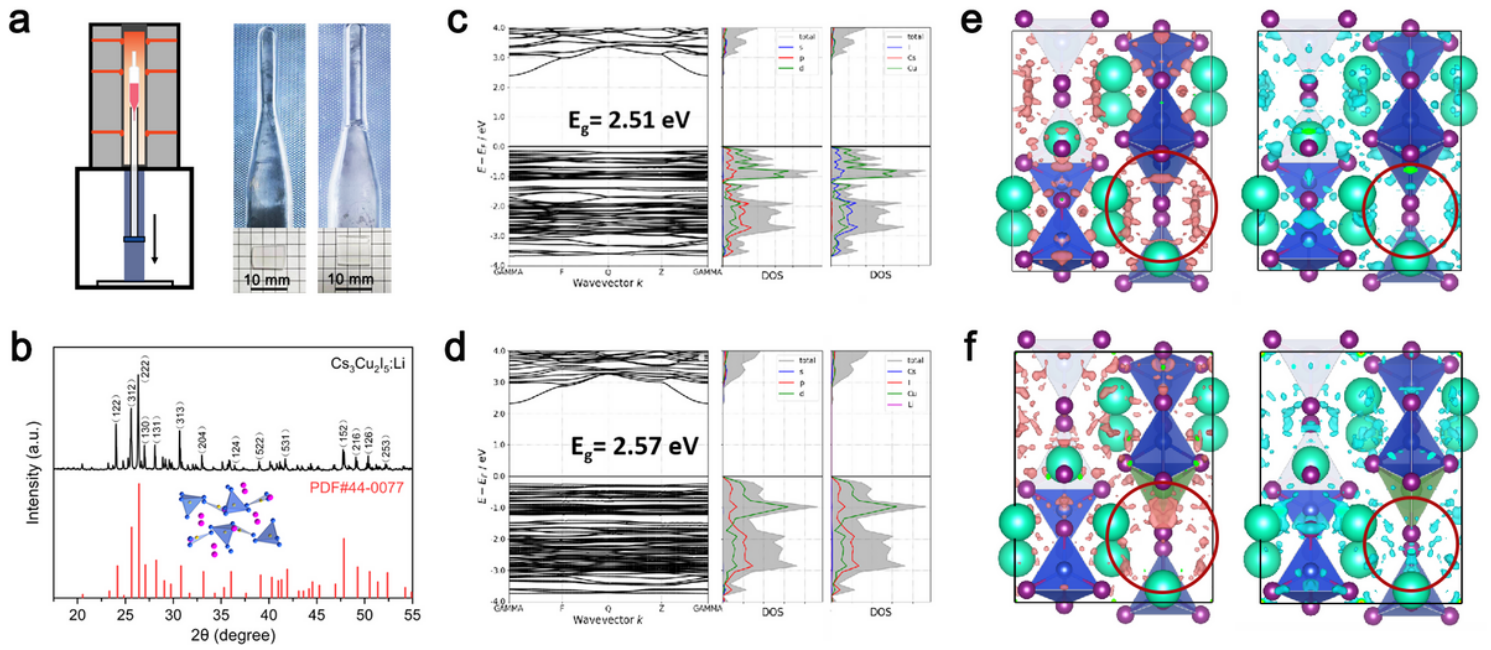
Figures

Figure 1

(a) Schematic diagram of the vertical Bridgman furnace for crystal growth and photographs of the as-grown $Cs_3Cu_2I_5$ and $Cs_3Cu_2I_5$:Li single crystals and machined samples. (b) Powder XRD pattern of $Cs_3Cu_2I_5$:Li. Electronic band structure of (c) pure and (d) Li^+-doped $Cs_3Cu_2I_5$. Charge density maps of VBM and CBM of (e) pure and (f) Li^+-doped $Cs_3Cu_2I_5$.
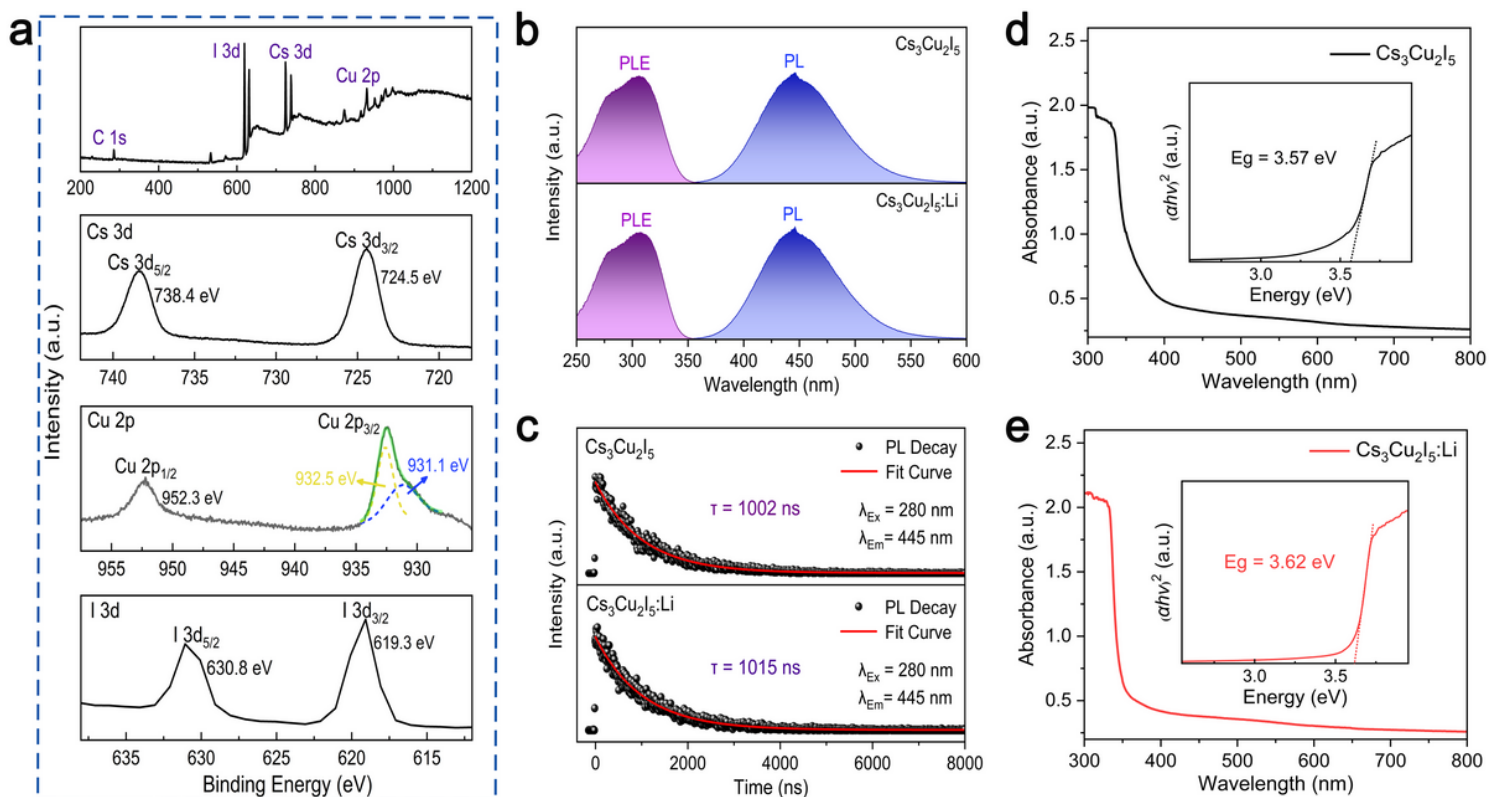
Figure 2

(a) XPS survey spectrum of $Cs_3Cu_2I_5$:Li and High-resolution XPS spectra of Cs 3d, Cu 2p and I 3d. (b) Photoluminescence emission and excitation spectra and (c) Decay profiles of pure and Li$^+$-doped $Cs_3Cu_2I_5$. Absorption spectra of (d) pure and (e) Li$^+$-doped $Cs_3Cu_2I_5$ (Inset: Tauc plot showing the direct bandgap).
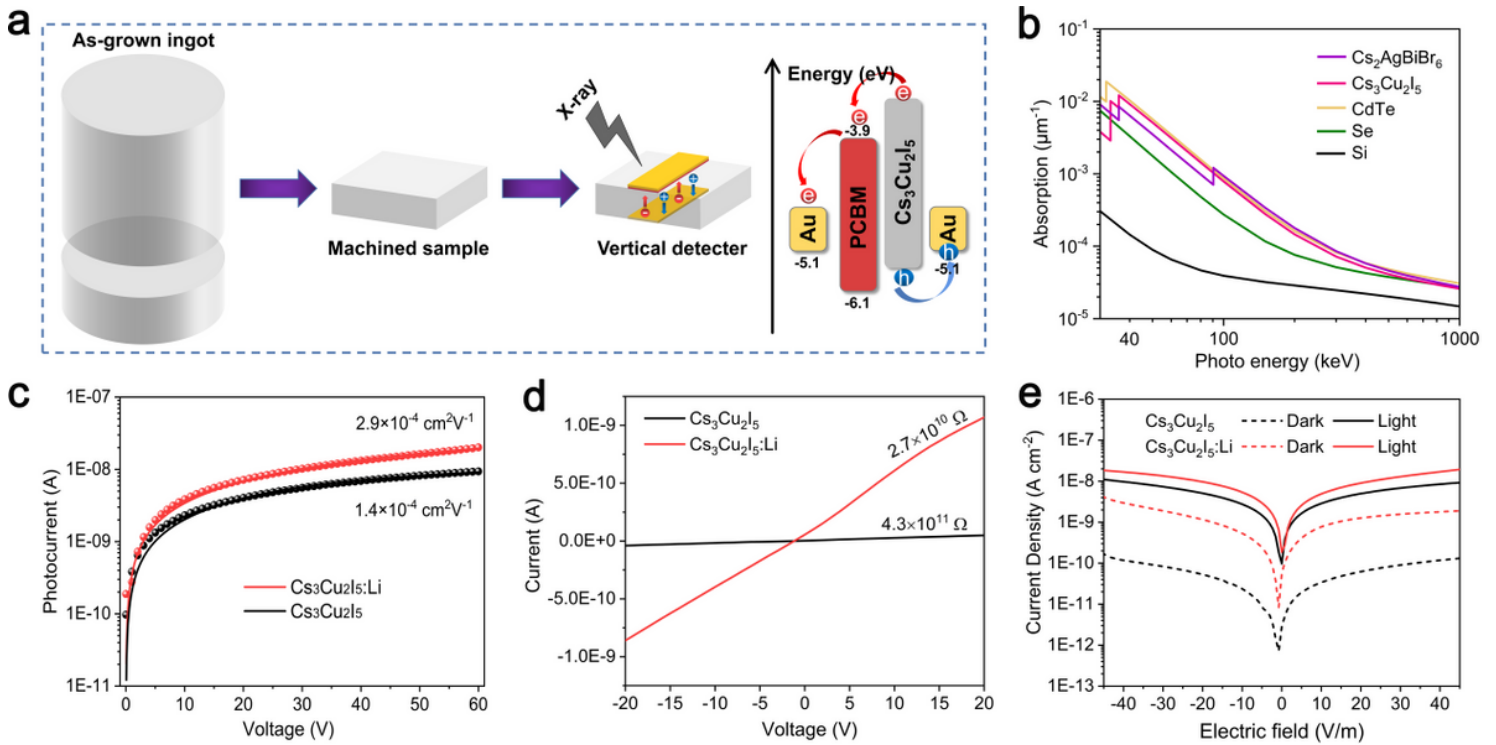

Figure 3

(a) Schematic of X-ray detector fabrication and device configuration, Calculated attenuation coefficient of various semiconductors for different X-ray energy (b), (c) Photoconductivity, (d) resistivity spectra of the $Cs_3Cu_2I_5$ and $Cs_3Cu_2I_5$:Li. (e) J-V characteristics of the $Cs_3Cu_2I_5$ and $Cs_3Cu_2I_5$:Li assisted X-ray detectors.
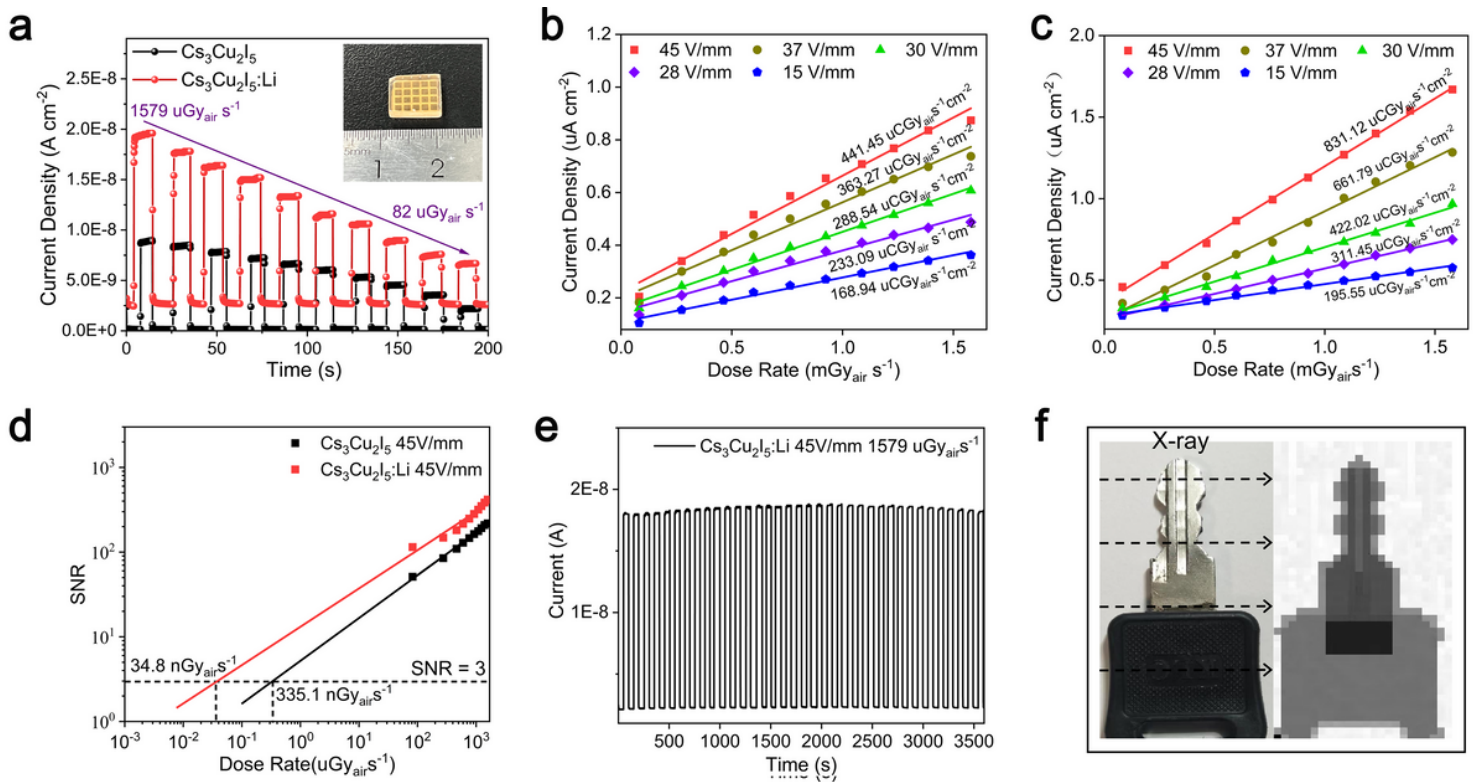
Figure 4

(a) X-ray response of the $Cs_3Cu_2I_5$ and $Cs_3Cu_2I_5$:Li assisted X-ray detectors and the picture of detector. Current densities generated by X-ray as a function of dose rates at different applied electrical fields for (b) $Cs_3Cu_2I_5$ and (c) $Cs_3Cu_2I_5$:Li detectors. (d) Dose rate dependent SNR of the detectors. (e) Stability of the $Cs_3Cu_2I_5$:Li detector under pulsed X-ray irradiation at a fixed dose rate. (f) Optical and X-ray images of a metallic key.

Supplementary Files

This is a list of supplementary files associated with this preprint. Click to download.

- SupportingInformation.docx